Stephan G. Jantz, Florian Pielnhofer and Henning A. Höppe*

On tungstates of divalent cations (III) – $Pb_5O_2[WO_6]$

https://doi.org/10.1515/zkri-2020-0041
Received April 16, 2020; accepted April 22, 2020; published online July 12, 2020

Abstract: $Pb_5O_2[WO_6]$ was discovered as a frequently observed side phase during our investigation on lead tungstates. Its crystal structure was solved by single-crystal X-ray diffraction ($P2_1/n$, $a = 7.4379(2)$ Å, $b = 12.1115(4)$ Å, $c = 10.6171(3)$ Å, $\beta = 90.6847(8)°$, $Z = 4$, $R_{int} = 0.038$, $R_1 = 0.020$, $\omega R_2 = 0.029$, 4188 data, 128 param.) and is isotypic with $Pb_5O_2[TeO_6]$. $Pb_5O_2[WO_6]$ comprises a layered structure built up by non-condensed $[WO_6]^{6-}$ octahedra and $[O_4Pb_{10}]^{12+}$ oligomers. The compound was characterised by spectroscopic measurements (Infrared (IR), Raman and Ultraviolet–visible (UV/Vis) spectra) as well as quantum chemical and electrostatic calculations (density functional theory (DFT), MAPLE) yielding a band gap of 2.9 eV fitting well with the optical one of 2.8 eV. An estimation of the refractive index based on the Gladstone-Dale relationship yielded $n \approx 2.31$. Furthermore first results of the thermal analysis are presented.

Keywords: crystal structure; lead; optical spectroscopy; tungstates; vibrational spectroscopy.

Dedicated to Professor Dr. Ulrich Müller on the occasion of his 80th birthday

1 Introduction

Tetrahedral moieties are the basic building unit of silicate-analogous materials. Normally, we are interested in materials classes such as borosulfates, *e.g.* $Pb[B_2O(SO_4)^3]$ [1], in which borate and sulphate tetrahedra form more or less condensed anionic frameworks interesting for optical properties. Chemically relatively closely related to sulfates are tungstates(VI) – often being present as WO_4 tetrahedra or WO_6 octahedra. In such transition metal centred polyhedra with the transition metal in high(est) oxidation states allowed ligand-to-metal charge transfer transitions (LMCT) are possible making them highly interesting as sensitisers or antennas for the excitation of otherwise poor absorbers like Eu^{3+}. Here, the $4f$–$4f$ excitations and emissions are parity forbidden and sensitisers help pumping and gaining intensity of such an emitter. Tungstates have been known for decades as efficient antenna phosphor host structures. Starting from bright red emitting $Y_2[WO_6]:Eu^{3+}$ till the recently described green emitter $YCl[WO_4]:Tb^{3+}$ [2, 3] many examples have been described.

In our first preceding contribution – essentially trying to combine silicate-analogous compounds with optically interesting tungstates – we came across the alkaline-earth tungstates $M_2[WO_5]$ (M = Sr, Ba) where a more or less crystallographic problem waited to be resolved for $Sr_2[WO_5]$. Besides that we could finally also observe red luminescence excited in the UV of trivalent europium ions doped onto the strontium sites [4].

The second preceding contribution on this topic we devoted to the lead tungstates Pb_2WO_5 where we elucidated the quite tricky phase-transition chemistry between the low temperature form Pb_2WO_5 and its high temperature counterpart $Pb_2O[WO_4]$. In Pb_2WO_5 chains of corner-sharing WO_6 octahedra host divalent lead cations, which upon heating transform into non-condensed WO_4 tetrahedra in $Pb_2O[WO_4]$; interestingly, herein the remaining oxygen atoms centre corner-sharing Pb_4 tetrahedra giving rise to infinite chains of the composition Pb_2O^{2+} [5]. Please note that non-infinitely condensed complex ions, *e. g.* in $Pb_2O[WO_4]$, are enclosed in brackets while infinite chains, *e.g.* in Pb_2WO_5, are not enclosed in brackets.

During the latter phase transition we frequently observed a side phase, and around its discovery, synthesis, first spectroscopic and thermal characterisation supported by density functional theory (DFT) calculations this third contribution on divalent main-group tungstates condenses. $Pb_5O_2[WO_6]$ is to some extent a perfect child to its parent compounds $Pb_2O[WO_4]$ and Pb_2WO_5. Regarding our

***Corresponding author: Henning A. Höppe**, Lehrstuhl für Festkörperchemie, Universität Augsburg, Universitätsstraße 1, 86159 Augsburg, Germany, E-mail: henning@ak-hoeppe.de. https://orcid.org/0000-0002-8734-8258
Stephan G. Jantz: Lehrstuhl für Festkörperchemie, Universität Augsburg, Universitätsstraße 1, 86159 Augsburg, Germany, E-mail: stephan@ak-hoeppe.de
Florian Pielnhofer: Institut für Anorganische Chemie, Universität Regensburg, 93053 Regensburg, Germany, E-mail: florian.pielnhofer@chemie.uni-regensburg.de

silicate-analogous chemistry herein in a sort of a topsy-turvy setting not tungsten centred tetrahedra but oxygen centred lead tetrahedra OPb_4 will be the maybe far-fetched connector to these important materials.

2 Results and discussion

2.1 Crystal structure description

On first glance, the crystal structure of $Pb_5O_2[WO_6]$ differs significantly from those of the *M* (II) tungstates $M_2[WO_5]$ (*M* = Sr, Ba, Pb) [4, 5]. Instead of forming zigzag chains of corner-sharing WO_6 octahedra, $Pb_5O_2[WO_6]$ crystallises isotypically to $Pb_5O_2[TeO_6]$ [6] in the monoclinic space group $P2_1/n$ (no. 14). The structure can be divided into an anionic partial structure built up by non-condensed $[WO_6]^{6+}$ octahedra and a cationic partial structure formed by $[O_4Pb_{10}]^{12+}$ oligomers (Figure 1, left). These are present in the structure in a ratio of 2 : 1 and form layers parallel to the (010) plane wherein the units alternate along [100] (Figure 1, right). The lead-oxygen oligomers are coordinated by the tungstate octahedra. On a second glance, the crystal structure of $Pb_5O_2[WO_6]$ adopts features of both parental phases – the WO_6 octahedra present in Pb_2WO_5 and the oxygen-centred Pb_4 tetrahedra found in $Pb_2O[WO_4]$.

The $[O_4Pb_{10}]^{12+}$ oligomer is formed by four edge-sharing OPb_4 tetrahedra (Figure 2), an excerpt from the layered crystal structure of PbO. The Pb–O distances within the tetrahedra are in the range 2.20–2.56 Å (∅ = 2.34 Å) and thus correspond on average to the sum of the effective ionic radii of 2.36 Å according to *Shannon* [7]. The O–Pb–O angles vary from 98.6–124.9Å (∅ = 109.4°). Further interatomic distances and angles are listed in Table 1. The deviation of the OPb_4 moieties from tetrahedral symmetry amounts to –4.62% and –2.44% for O7 and O8, respectively. It was calculated employing the method of Balić-Žunić and Makovicky based on all ligands enclosing spheres on experimental data [8, 9].

Similar to the above mentioned *M*(II) tungstates, the WO_6 octahedron in $Pb_5O_2[WO_6]$ (Figure 3, left) shows a significant out-of-centre distortion, which is observed frequently in octahedrally coordinated d^0 transition metal ions [10]. The average W–O distance of 1.94 Å matches very well with the sum of the effective ionic radii of 1.97 Å [7]; this average is yielded from distances in the quite large range 1.79–2.18 Å (Table 1), though. The O–W–O angles are in the range 78.7–100.5Å (adjacent oxygen atoms; ∅ = 89.8°) and 162.2–170.6° (opposite oxygen atoms; ∅ = 167.7°).

The coordination of the five crystallographically distinct lead atoms is visualised in Figure 3 (right). Pb1 and Pb3 are coordinated four-fold by oxygen atoms forming a singly capped trigonal pyramid. Pb2, Pb4 and Pb5 are coordinated five-fold by oxygen atoms building twice capped trigonal pyramids. The Pb–O distances in these coordination environments range from 2.20–2.87 Å (∅ = 2.44 Å). On average the Pb–O distances between the O_4Pb_{10} oligomers and the WO_6 octahedra (dashed grey lines in Figure 1, right) are larger (∅ = 2.49 Å) in comparison to those within the OPb_4 tetrahedra (∅ = 2.34 Å). Apparently, the environment of the lead atoms is quite asymmetric due to a strong lone-pair effect; the three empty *p* orbitals give frequently rise to three relatively short Pb–O bonds with angles close to 90 and an according tripod coordination for these three shortest partners (most convincingly seen in the case of Pb1, Pb3 and Pb4) – and no ligands closely bound to the backbone side. Such behaviour is well known for s^2 ions like in $SnB_2O_3F_2$ – and confirmed by calculations on $Sn(OH_2)_3^{2+}$ [11, 12].

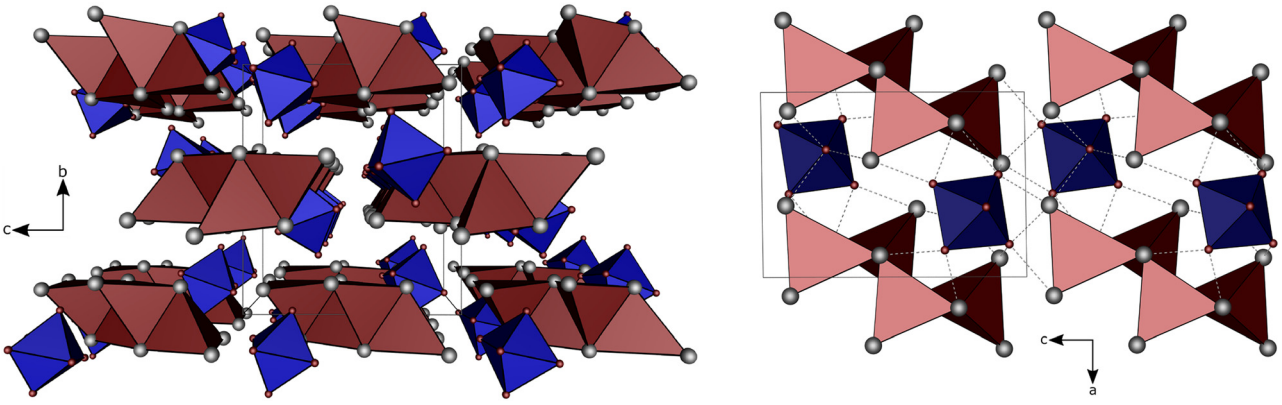

Figure 1: Crystal structure of $Pb_5O_2[WO_6]$ along [100]; central projection; lead grey, oxygen red, WO_6 octahedra blue, OPb_4 tetrahedra red (left); crystal structure of $Pb_5O_2[WO_6]$ along [010]; lead grey, oxygen red, WO_6 octahedra blue, OPb_4 tetrahedra red; the dashed grey lines depict Pb–O bonds with distances of 2.21–2.87 Å (right).

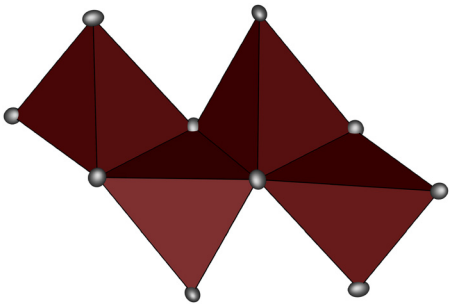

Figure 2: The $[O_4Pb_{10}]^{12+}$ oligomer in $Pb_5O_2[WO_6]$; OPb_4 tetrahedra red, lead atoms (grey) are drawn with their displacement ellipsoids at a 75% probability level.

Our description of the Pb-coordination deviates from that given by *Artner* and *Weil* for the isotypic $Pb_5O_2[TeO_6]$ [6]. While they state lead coordination numbers of six and eight with Pb–O distances of 2.20–3.55 Å, we considered only distances up to 3.0 Å, based on our MAPLE and ECoN (Table S1) calculations on $Pb_5O_2[WO_6]$.

2.2 Electrostatic Calculations

We checked the structure model of $Pb_5O_2[WO_6]$ for electrostatic reasonability using calculations based on the MAPLE concept (MAPLE = Madelung Part of Lattice Energy) [13–15]. A structure model is considered as electrostatically consistent if the sum of MAPLE values of chemically similar compounds deviates from the MAPLE value of the compound of interest by less than 1%. According to our calculations the structure model thus shows electrostatic consistency (Table 2). Also the contribution of the oxygen atoms to the coordination environment of the lead atoms was confirmed by ECoN calculations (Table S1 in the Supplement). Thus only oxygen atoms comprising Pb–O distances up to 3.0 Å contribute significantly.

2.3 Infrared and Raman spectroscopy

The InfraRed (IR) and Raman spectra of $Pb_5O_2[WO_6]$ (Figure 4) were recorded between 4000 and 400 cm^{-1} (IR) and 3500–50 cm^{-1} (Raman) on powder samples. Above 1000 cm^{-1} no absorption bands were recorded in both spectra. These are quite similar to the spectra of Pb_2WO_5 [5], what is not further surprising due to the presence of nearly the same building units. The band positions and the respective assignment based on our DFT calculations (see section 2.5) are summarised in Table 3. Although the calculated band positions are shifted relatively to the observed ones, the assignment becomes clear from the energetic gaps between the groups. $Pb_5O_2[WO_6]$ comprises symmetric stretching vibrations of the WO_6 octahedra at 825 cm^{-1} (IR) and 835 cm^{-1} (Raman). The vibrations in the region 750–500 cm^{-1} can be assigned to the asymmetric stretching vibrations of the WO_6 octahedra. Below 475 cm^{-1} follow several deformation and lattice vibrations.

Table 1: Relevant ranges of interatomic distances/Å and angles/° in $Pb_5O_2[WO_6]$ (esds in parentheses).

Atoms	CN	Distance/Å	∅/Å
Pb1–O	4	2.230(2)–2.714(3)	2.44(20)
Pb2–O	5	2.296(2)–2.640(3)	
Pb3–O	4	2.231(2)–2.773(3)	
Pb4–O	5	2.198(2)–2.760(2)	
Pb5–O	5	2.214(2)–2.871(3)	
O–Pb[a]		2.214(2)–2.871(3)	2.49(21)
O7–Pb	4	2.198(2)–2.564(3)	2.34(12)
O8–Pb	4	2.296(2)–2.416(2)	
W1–O	6	1.785(3)–2.179(3)	1.94(13)
Atoms		**Angle/°**	**∅/°**
Pb–O7–Pb		98.55(9)–119.15(10)	109.4(8.2)
Pb–O8–Pb		98.85(9)–124.90(10)	
O–W1–O[b]		78.74(10)–100.51(13)	89.8(6.4)
O–W1–O[c]		162.23(11)–170.56(11)	167.7(3.9)

[a]Only O1–O6 are considered
[b]Adjacent neighbours
[c]Opposite neighbours

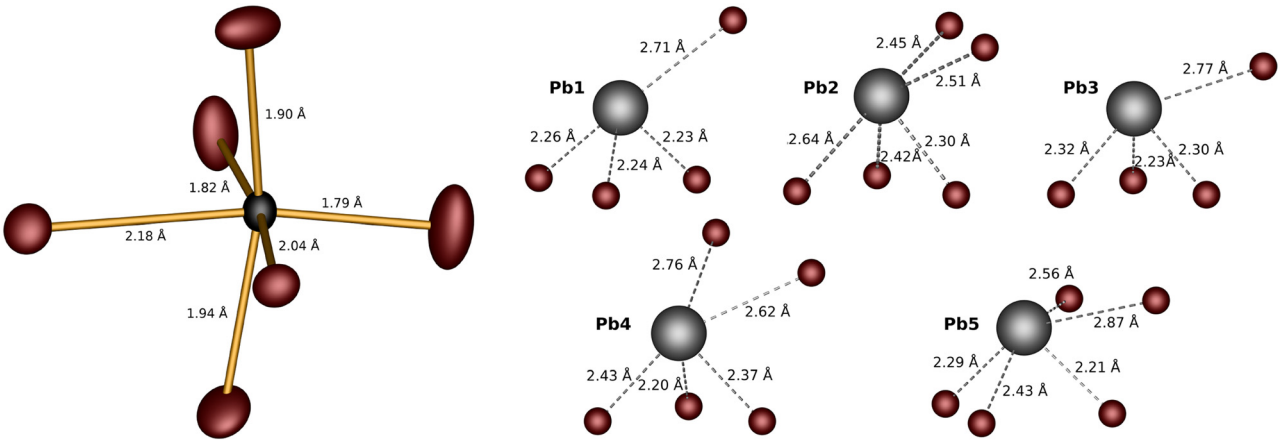

Figure 3: The WO_6 octahedra in $Pb_5O_2[WO_6]$; tungsten blue, oxygen red; all atoms are drawn with their displacement ellipsoids at a 75% probability level (left); coordination environments of the lead atoms in $Pb_5O_2[WO_6]$; lead grey, oxygen red (right) – for the sake of better clarity the interatomic distances were rounded.

2.4 UV–Vis Spectroscopy

The Ultraviolet–visible (UV–Vis) reflectance spectrum of $Pb_5O_2[WO_6]$ (Figure 5) reveals an absorption edge centred at 440 nm which corresponds very well with its yellow body colour and an optical band gap at approximately 2.8 eV. This is in perfect agreement with the results of our DFT calculations (see section 2.5) which yielded a band gap of 2.9 eV. Accordingly, the band gap of $Pb_5O_2[WO_6]$ ranges in the regime of that of *massicot* of 2.7 eV [18]. The average refractive index of the title compound can be estimated via revised increments [19] employing the relationship found by *Gladstone* and *Dale* for liquids [20] and transferred onto minerals by *Larsen* [21]:

$$n \approx 1 + \rho\sum p_i k_{r,i} = 1 + 9.361\left(0.828 \cdot 0.133^{\mathrm{PbO}} + 0.172 \cdot 0.171^{\mathrm{WO_3}}\right) \approx 2.31$$

with the density determined from the single-crystal structure determination, the increments $k_{r,i}$ for all components with respective weight-percentages p_i.

Attempts to dope $Pb_5O_2[WO_6]$ with europium ions were not successful as all samples which contained an europium source showed large amounts of side-phases and no reliable indication for a successful doping of the title compound with europium.

Table 2: Result of the MAPLE calculations for $Pb_5O_2[WO_6]$ compared with the MAPLE calculations on α – PbO (ICSD no. 15403) [16] and WO_3 (ICSD no. 16080) [17].

Compound	MAPLE/kJ mol^{-1}
α – PbO	3636
WO_3	26,087
5 α – PbO + WO_3	44,267
$Pb_5O_2[WO_6]$	44,356
$\Delta = 0.20\%$	

2.5 DFT calculations

DFT calculations with different functionals (LDA, GGA(PBE), HSE06) were performed in order to interpret the vibrational spectra and to study the electronic structure of the title compound. The cell volume is underestimated by 6.8% with the LDA functional and overestimated by 5.3% with GGA and 4.3% with HSE06. Optimised lattice parameters are listed in Table 4. Vibrational spectra were simulated based on the GGA structure optimization.

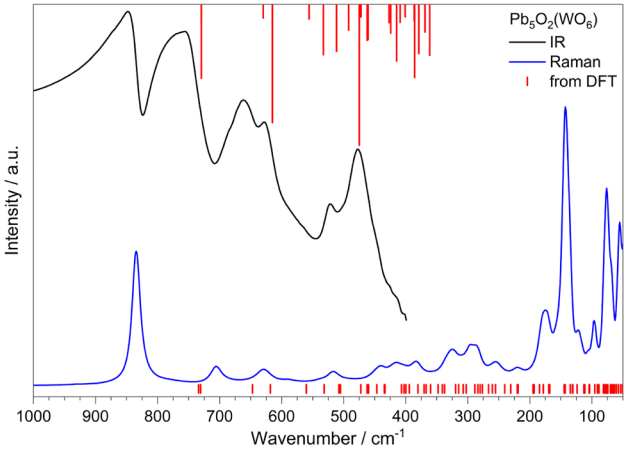

Figure 4: InfraRed (IR) (black) and R (Raman) (blue) spectra of $Pb_5O_2[WO_6]$; the red bars represent the respective IR and R modes calculated by DFT.

Table 3: Observed IR- and Raman- bands of $Pb_5O_2[WO_6]$ and their respective assignment derived from density functional theory (DFT).

IR/cm^{-1}	Raman/cm^{-1}	Assignment
825	835	$\nu_s(WO_6)$
708	706	$\nu_{as}(WO_6)$
638, 595	630	$\nu_{as}(WO_6)$
545, 510	516	$\nu_{as}(WO_6)$
<475	<475	$\delta(WO_6)$, lattice vibrations

Table 4: Lattice parameters, cell volumes and band gaps obtained with the different functionals in comparison to experimental values.

	a/Å	*b*/Å	*c*/Å	*β*/°	*V*/Å^3	E_G/eV
Exp	7.438	12.112	10.617	90.68	956.36	2.8
LDA	7.426	11.542	10.399	89.62	891.30	1.6
GGA	8.116	11.650	10.648	90.48	1006.70	1.9
HSE	7.946	11.968	10.489	89.02	997.34	2.9

It is well known for the standard DFT functionals LDA and GGA to underestimate bandgaps, which is also obtained in this study. 1.6 eV (LDA) and 1.9 eV (GGA) extremely deviate from the value of 2.8 eV which was determined by UV/VIS spectroscopy. However, the inclusion of exact Fock exchange with the hybrid functional HSE06 reproduces the experimental optical bandgap very well (see Table 4). The valence band of $Pb_5O_2[WO_6]$ is mainly composed of O-2*p* states but minor contributions of W-5*d* and Pb-6*s* are also found directly below the Fermi level. W-5*d* states primarily and less contributions of O-2*p*, O-2*s*, Pb-6*p* and Pb-6*s* form the conduction band (see Figure 6).

2.6 Thermal analysis

The TGA curve of $Pb_5O_2[WO_6]$ was recorded up to 1400 Â°C under nitrogen atmosphere. In the measured range it comprises a single step representing a mass loss of 56.1% starting at approx. 890 °C. As the decomposition was not finished at the maximum temperature and the sample had a glassy appearance after the TGA measurement, which hindered the powder XRD analysis of the residue to deliver any proof of a crystalline phase, we have no reliable information about the decomposition products. The TGA curve is depicted in Figure S1 in the supplement.

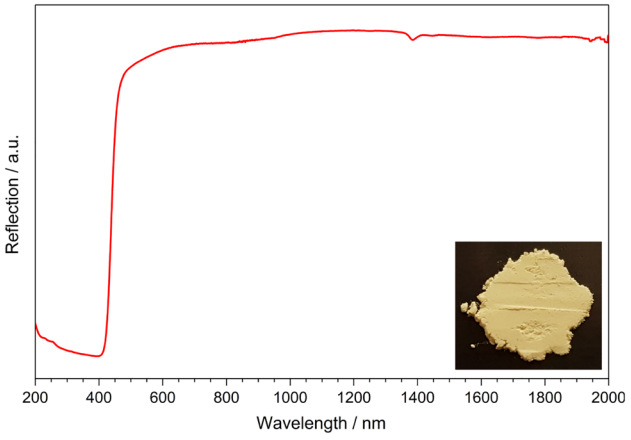

Figure 5: Ultraviolet–visible (UV–Vis) reflectance spectrum of $Pb_5O_2[WO_6]$; the inset shows the photograph of a sample.

3 Conclusion

As mentioned at the end of the introduction, $Pb_5O_2[WO_6]$ is indeed to some extent a perfect child to its parent compounds $Pb_2O[WO_4]$ and Pb_2WO_5: Single-crystals of $Pb_5O_2[WO_6]$ were obtained from a 1 : 1 mixture of both phases Pb_2WO_5 [5] under assistence of LiF as flux. $Pb_5O_2[WO_6]$ crystallises isotypically with $Pb_5O_2[TeO_6]$ [6] and comprises WO_6 octahedra featuring the first parent – but here they are non-condensed in contrast to Pb_2WO_5 – and condensed OPb_4 tetrahedra featuring the second $Pb_2O[WO_4]$ – but here condensed via common edges to give oligomers of the composition $[O_4Pb_{10}]^{12+}$ instead of infinite chains. The optical band-gap of 2.8 eV matches well with the calculated one of 2.9 eV and is in line with a slightly smaller one of *massicot* – in which the condensation of the lead-oxygen framework is infinite while here only oligomers are present.

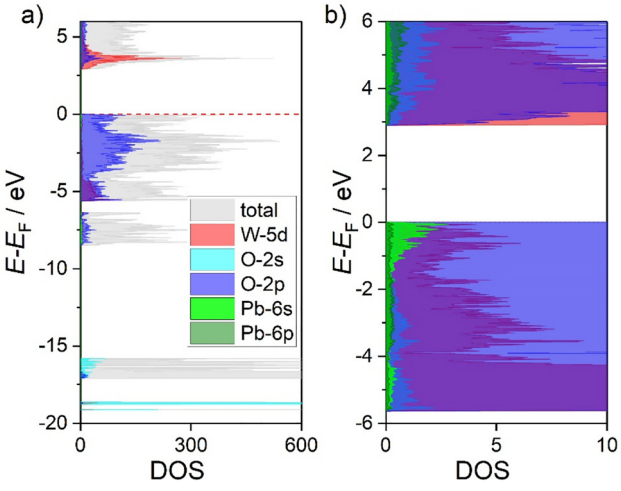

Figure 6: a) Atomic orbital projected density of states (PDOS) for all valence electrons and b) zoom into the valence and conduction band region (HSE06 calculations).

Table 5: Crystal data and details of the structure refinement on $Pb_5O_2[WO_6]$

Sum formula	$Pb_5O_2[WO_6]$	Diffractometer	Bruker D8 Venture
M/g·mol^{-1}	1347.80	Radiation | λ/Å	Mo-K_α | 0.71073
Crystal system	monoclinic	Temperature/K	283(2)
Space group	$P2_1/n$ (no. 14)	Index range h | k—l	±12 | ±19 | ±17
a/Å	7.4379(2)	Theta range/°	$2.551 \le \theta \le 34.994$
b/Å	12.1115(4)	Collected reflections	35,645
c/Å	10.6171(3)	Indexed data	4188
β/°	90.6847(8)	Observed refl. ($I > 2\sigma$)	3809
V/Å^{-3}	956.36	Absorption correction	multi-scan
Z	4	Transmission min./max.	0.3641/0.7494
ρ_{X-ray}/g·cm^{-3}	9.36	R_{int}, R_σ	0.038, 0.020
Refined Parameters | Restraints		128 | 0	
R_1 (all Data), ωR_2 (all Data)		0.020, 0,029	
Weighting scheme		$\omega^{-1} = \sigma^2 F_o^2 + (0.0080P)^2 + 1.2861P$; $P = (F_o^2 + 2F_c^2)/3$	
GooF		1.097	
Resid. el. dens. min./max./e$^-$·Å^{-3}		−1.58/2.85	

4 Experimental section

4.1 Synthesis

A polycrystalline powder of $Pb_5O_2[WO_6]$ was obtained from the mixture of PbO (≥99%, Riedel-de Haën) and WO_3 (99.9%, Fluka) in a molar ratio of 5:1. The starting materials were ground thoroughly and filled into a silver crucible, which was further encapsulated in an evacuated silica ampoule. The sample was heated to 650 °C with a heating rate of 100 °C/h in an electric furnace. The sample was held at this temperature for 24 h before it was cooled to room temperature with 200 °C/h. This resulted in a finely crystalline yellowish powder, which was proven to be single-phase by powder X-ray diffraction (Figure S2 in the Supplement).

Single-crystals of $Pb_5O_2[WO_6]$ were obtained from a 1:1 mixture of Pb_2WO_5 (mixture of both phases, cf. *Jantz* et al. [5]) and LiF (97%, Fluka). The starting materials were ground thoroughly and heated to 800 °C with a heating rate of 100 °C/h using Al_2O_3 crucibles. After maintaining this temperature for 24 h the sample was cooled to room temperature with 300 °C/h. This sample contained several side phases beside the single-crystals of the target compound.

4.2 Crystal structure determination

A suited crystal of $Pb_5O_2[WO_6]$ was selected under an optical microscope equipped with crossed polarisation filters and mounted on a MicroMount (MiTeGen). Single-crystal X-ray diffraction data were collected on a Bruker D8 Venture diffractometer equipped with a SMART APEXII 4k CCD detector, using Mo-K_α radiation. In total 35,645 reflections were collected. Out of 4188 unique reflections, 3809 reflections were observed ($F_o^2 > 2\sigma(F_o^2)$, $R_{int} = 0.038$). The data were corrected for absorption by applying a multi-scan approach and solved by direct methods using the SHELXTL program package [22]. The refinement was carried out with anisotropic displacement parameters for all atoms. Details of the X-ray data collection and the refinement are summarised in Table 5. The positional and displacement parameters for all atoms are listed in the Supplement (Tables S2 and S3); further details of the crystal structure investigation of $Pb_5O_2[WO_6]$ may be obtained from the Fachinformationszentrum Karlsruhe, D-76344 Eggenstein-Leopoldshafen, Germany (E-mail: crysdata@fiz-karlsruhe.de) on quoting the depository number CSD−1997,063, the names of the authors, and citation of this publication.

4.3 Powder X-ray diffraction

The phase purity of the powder samples of $Pb_5O_2[WO_6]$ was checked by powder X-ray diffraction(PXRD) (Figure S2). The patterns were recorded on a Seifert XRD T/T 3003 diffractometer in reflection geometry equipped with a Meteor 1D linear detector.

4.4 Density functional theory calculations

Quantum chemical calculations were performed in the framework of density functional theory (DFT) using a linear combination of Gaussian-type functions (LCGTF) scheme as implemented in CRYSTAL14/17 [23–26]. Full structural optimizations were performed at different levels of theory using various functionals: LDA(VWN) [27], GGA (PBE) [28] and HSE06 [29, 30]. The convergence criterion considering the energy was set to $1 \cdot 10^{-8}$ a.u. with a k-mesh sampling of $8 \times 8 \times 8$ in LDA and GGA calculations. Less strict convergence criteria of $1 \cdot 10^{-7}$ a.u. with $6 \times 6 \times 6$ k-points were employed in the more costly HSE06 calculations. Optimized effective core potential basis sets were applied for Pb and W [31, 32], the description of the O-atoms was carried out by an all-electron basis [33]. The vibrational frequencies were

computed on the basis of the relaxed structure (GGA). The modes were visualized and analysed with the J-ICE application [34].

4.5 Spectroscopy

IR spectra were recorded on a Bruker EQUINOX 55 Fourier Transform InfraRed (FT-IR)-Spectrometer equipped with a Platinum ATR unit in the range 4000–400 cm^{-1} with a resolution of 4 cm^{-1} and 32 scans.

Raman spectra were recorded on a Thermo Scientific DXR Raman-Microscope in the range 3500–50 cm^{-1} using a 532 nm laser operated with 10 mW power (10–fold magnification, 50 µm pinhole aperture, standard resolution grating (900 lines mm^{-1}), spectral resolution 2 cm^{-1}).

UV–V is spectra were recorded in reflection geometry on a PerkinElmer Lambda 750S UV–V is spectrometer.

4.6 Thermal analysis

Thermogravimetricanalysis (TGA) measurements were conducted on a Netzsch STA 409 PC Luxx thermal analyser in a temperature range up to 1400 °C in corundum crucibles. The experiment was recorded under inert atmosphere (N_2) with a flow rate of 50 mL min^{-1}.

Acknowledgement: F.P. thanks Prof. Bettina Lotsch, Dr. Ulrich Wedig and the Computer Service group from the Max-Planck-Institute for Solid State Research (Stuttgart, Germany) for access to CRYSTAL17 and computational facilities.

Author contribution: All the authors have accepted responsibility for the entire content of this submitted manuscript and approved submission.

Research funding: None declared.

Conflict of interest statement: The authors declare no conflicts of interest regarding this article.

References

1. Netzsch P., Gross P., Takahashi H., Lotfi S., Brgoch J., Höppe H. A. *Eur. J. Inorg. Chem.* 2019, *36*, 3975–3981.
2. Blasse G., Bril A. *J. Chem. Phys.* 1966, *45*, 2350–2355.
3. Schustereit T., Netzsch P., Höppe H. A., Hartenbach I. *Z. Anorg. Allg. Chem.* 2018, *644*, 1749–1753.
4. Jantz S. G., Pielnhofer F., Dialer M., Höppe H. A. *Z. Anorg. Allg. Chem.* 2017, *643*, 2024–2030.
5. Jantz S. G., Pielnhofer F., Dialer M., Höppe H. A. *Z. Anorg. Allg. Chem.* 2017, *643*, 2031–2037.
6. Artner C., Weil M. *J. Solid State Chem.* 2013, *199*, 240–247.
7. Shannon R. D. *Acta Crystallogr.* 1976, *B32*, 751–767.
8. Balić-Žunić T., Makovicky E. *Acta Crystallogr. B* 1996, *52*, 78–81.
9. Makovicky E., Balić-Žunić T. *Acta Crystallogr. B* 1998, *54*, 766–773.
10. M. Kunz, Brown I. D. *J. Solid State Chem.* 1995, *115*, 395–406.
11. Jantz S. G., Dialer M., Bayarjargal L., Winkler B., van Wüllen L., Pielnhofer F., Brgoch J., Weihrich R., Höppe H. A. *Adv. Opt. Mater.* 2018, *6*, 1800497.
12. Klüfers P. "Personal communication", calculation of $[Sn(H_2O)_3]^{2+}$ on BP86/def2- tzvp niveau (van-der-Waals correction, modelled aqueous environment) yields antibonding Sn-O interactions besides *s* contribution of Sn and an O-Sn-O angle of approx. 78.5°.
13. Hoppe R. *Angew. Chem. Int. Ed.* 1966, *5*, 95–106.
14. Hoppe R. *Angew. Chem. Int. Ed.* 1970, *9*, 25–34.
15. Hübenthal R. *MAPLE Program for the Calculation of the Madelung Part of Lattice Energy*; Justus-Liebig-University Giessen: Germany, 1993.
16. Kay M. *Acta Crystallogr.* 1961, *14*, 80–81.
17. Loopstra B. O., Rietveld H. M. *Acta Crystallogr. B* 1969, *25*, 1420–1421.
18. Demkov A., Navrotsky A. *Materials Fundamentals of Gate Dielectrics*; Springer Netherlands: Dordrecht, 2006.
19. Mandarino J. A. *Can. Mineral.* 1981, *19*, 441–450.
20. Gladstone J. H., Dale T. P. *Philos. Trans. Roy. Soc. London* 1863, *153*, 317–343.
21. Larsen E., Geological Survey U.S. *The Microscopic Determination of the Nonopaque Minerals*; U.S. Government Printing Office: Washington, DC, 1921.
22. Sheldrick G. *Acta Crystallogr. B* 2008, *64*, 112–122.
23. Dovesi R., Saunders V. R., Roetti C., Orlando R., Zicovich-Wilson C. M., Pascale F., Civalleri B., Doll K., Harrison N. M., Bush I. J., D'Arco P., Llunel M., Causà M., Noël Y., Maschio L., Erba A., Rérat M., Casassa S. *CRYSTAL14 User's Manual*; University of Torino: Torino, Italy, 2014.
24. Dovesi R., Orlando R., Erba A., Zicovich-Wilson C. M., Civalleri B., Casassa S., Maschio L., Ferrabone M., Pierre M. D. L., D'Arco P., Noël Y., Causà M., Rérat M., Kirtman B. *Int. J. Quantum Chem.* 2014, *114*, 1287–1317.
25. Dovesi R., Erba A., Orlando R., Zicovich-Wilson C. M., Civalleri B., Maschio L., Rérat M., Casassa S., Baima J., Salustro S., Kirtman B. *WIRes: Comp. Mol. Sci.* 2018, *8*, e1360.
26. Dovesi R., Saunders V. R., Roetti C., Orlando R., Zicovich-Wilson C. M., Pascale F., Civalleri B., Doll K., Harrison N. M., Bush I. J., D'Arco P., Llunel M., Causà M., Noël Y., Maschio L., Erba A., Rérat M., Casassa S. *CRYSTAL17 User's Manual*; University of Torino: Torino, Italy, 2017.
27. Vosko S. H., Wilk L., Nusair M. *Can. J. Phys.* 1980, *58*, 1200–1211.
28. Perdew J. P., Burke K., Ernzerhof M. *Phys. Rev. Lett.* 1996, *77*, 3865–3868.
29. Becke A. D. *Phys. Rev. A* 1988, *38*, 3098–3100.
30. Heyd J., Scuseria G. E., Ernzerhof M. *J. Chem. Phys.* 2003, *118*, 8207–8215.
31. Sophia G., Baranek P., Sarrazin C., Rérat M., Dovesi R. *Phase Trans.* 2013, *86*, 1069–1084.
32. ECP60MHF *Basis set ECP60MHF for W*; University of Cologne: Germany. http://www.tc.uni-koeln.de/PP/clickpse.en.html.
33. Scaranto J., Giorgianni S. *J. Mol. Struct.: Theochem* 2008, *858*, 72–76.
34. Canepa P., Hanson R. M., Ugliengo P., Alfredsson M. *J. Appl. Crystallogr.* 2014, *44*, 225–229.

Supplementary Material: The online version of this article offers supplementary material (https://doi.org/10.1515/zkri-2020-0041).